Bulletin of Geophysics and Oceanography Vol. 67, n. 3, pp. 553-580; September 2026
DOI 10.4430/bgo00529

On the currents and water masses on the shelf break SW of Spitsbergen

P-M. Poulain[1,*] and C. Lathuilière[2]

[1] *NATO Science and Technology Organization, Centre for Maritime Research and Experimentation - CMRE, La Spezia, Italy*
[2] *Naval Hydrographic and Oceanographic Service - SHOM, Brest, France*
[*] *Now at National Institute of Oceanography and Applied Geophysics – OGS, Trieste, Italy*

(Received: 28 August 2025; accepted: 20 February 2026; published online: 7 July 2026)

ABSTRACT A multi-platform observational campaign to investigate sea level, currents, and thermohaline properties near the shelf break was conducted SW of Spitsbergen in early autumn 2019. Using moored and mobile instruments, we captured variability on timescales between 12 hours and a few days with high spatial resolution. Sea level estimates revealed dominant semidiurnal tidal constituents, with amplitudes up to 84 cm. Acoustic Doppler current profiler and drifter data confirmed the presence of the West Spitsbergen Current along the slope but also highlighted weak SE-ward mean currents on the shelf. Tidal currents, particularly the M2 and K1 constituents, accounted for a large portion of velocity variance, with cross-shelf transport indicated by low-eccentricity tidal ellipses. Water column structure showed baroclinic tidal flows, with depth-dependent current variations and the presence of an internal tide. Drifter data confirmed enhanced near-surface variability, likely influenced by near-inertial motions. High-frequency thermohaline measurements from a Wirewalker profiler revealed a periodically varying mixed layer, pronounced internal tide signatures, and dynamic interactions between colder, fresher Arctic Water and warmer, saltier Atlantic Water across the polar front. Glider observations confirmed these thermohaline structures and further highlighted the spatial complexity induced by tidal modulation and fine-scale interleaving of the two water masses.

Key words: Spitsbergen shelf, polar front, water masses, tidal currents, moorings, gliders, drifters, Wirewalker.

1. Introduction

The West Spitsbergen Current (WSC) is vital to the global thermohaline circulation and Arctic climate, as it transports warm, saline waters into the Arctic Ocean via the Fram Strait (see Fig. 1). The WSC has two main branches (Gascard *et al.*, 1995; Orvik and Niiler, 2002; Teigen *et al.*, 2010, 2011). The eastern WSC is a robust, predominantly barotropic northward current constrained by the continental bathymetric slope (200–1,000 m isobaths) between the deep Norwegian Sea to the west and the Barents Sea and Spitsbergen shelf to the east. The offshore western branch of the WSC flows northwards along the base of the topographic slope. Though weaker and more variable, it is influenced by frequent mesoscale eddies and meanders (Gascard *et al.*, 1995; Teigen *et al.*, 2010).

The polar front (PF) in the eastern Fram Strait separates two distinct water masses: the warm

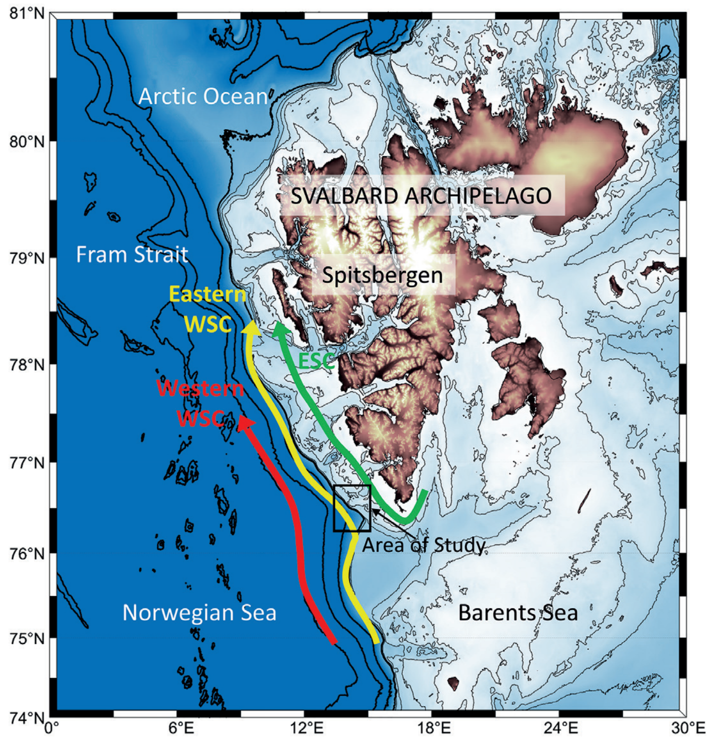

Fig. 1 - The Svalbard Archipelago, including Spitsbergen, with the bathymetry of the surrounding seas. The study area is highlighted within a rectangle. Isobaths are depicted at 100, 200, 300, and 400 m (thin lines), and at 500, 1,000, 1,500, and 2,000 m (thick lines). The main currents in the vicinity of the study area are shown schematically: the western branch of the WSC in red, the eastern branch of the WSC in yellow, and the ESC in green.

Atlantic Water (AW) offshore in the two WSC branches and the colder, fresher Arctic Water (ArW) on the continental shelf (Figs. 1 and 2). The eastern WSC has been extensively studied (e.g. Quadfasel *et al.*, 1987; Gascard *et al.*, 1995; Boyd and d'Asaro, 1994; Saloranta and Svendsen, 2001; Teigen *et al.*, 2010, 2011). Regarding the properties and origins of the shelf waters, it is believed that ArW (and, seasonally, sea ice) rounds the southern tip of Spitsbergen, an island of the Svalbard archipelago, and is transported northwards by the East Spitsbergen Current (ESC) on the shelf (see Fig. 1; Loeng, 1991; Saloranta and Svendsen, 2001). East of the PF, the cooler and fresher ArW [see the sea surface temperature (SST) map in Fig. 2] is influenced by sea-ice formation and melting on the shelf and in the Spitsbergen's main fjords (Bensi *et al.*, 2019).

Lagrangian drifters have shown that near-surface currents in the eastern WSC can exceed 40 cm/s (Poulain *et al.*, 1996; Koszalka *et al.*, 2011; Poulain, 2025). In contrast, the mean northward ESC flow on the Spitsbergen shelf is limited to 5–10 cm/s. The eastern WSC can become unstable, generating oscillations and meanders through barotropic and baroclinic instability processes (Teigen *et al.*, 2010, 2011; Nilsen *et al.*, 2016). These instabilities have typical wavelengths of 15–40 km and periods of 35–75 hours (Teigen *et al.*, 2010, 2011). Such oscillations facilitate cross-shelf exchange of heat and salt between the AW and ArW, with mesoscale variability peaking in winter (Von Appen *et al.*, 2016). Barotropic meandering is also modulated by the slope and shelf bottom topography, with variations linked to the morphology of nearby fjords (Nilsen *et al.*, 2016).

In addition to the strong WSC and its instabilities (meanders and pinched-off eddies), as well as the weaker ESC, the currents west of Spitsbergen fluctuate over shorter timescales due to tidal forcing. Diurnal and semidiurnal currents, with speeds reaching ~5 cm/s, have been observed using moored current meters (Kasajima and Svendsen, 2002) and drifters (Poulain, 2025), and have been simulated numerically (Kowalik and Proshutinsky, 1993; Gjevik *et al.*, 1994;

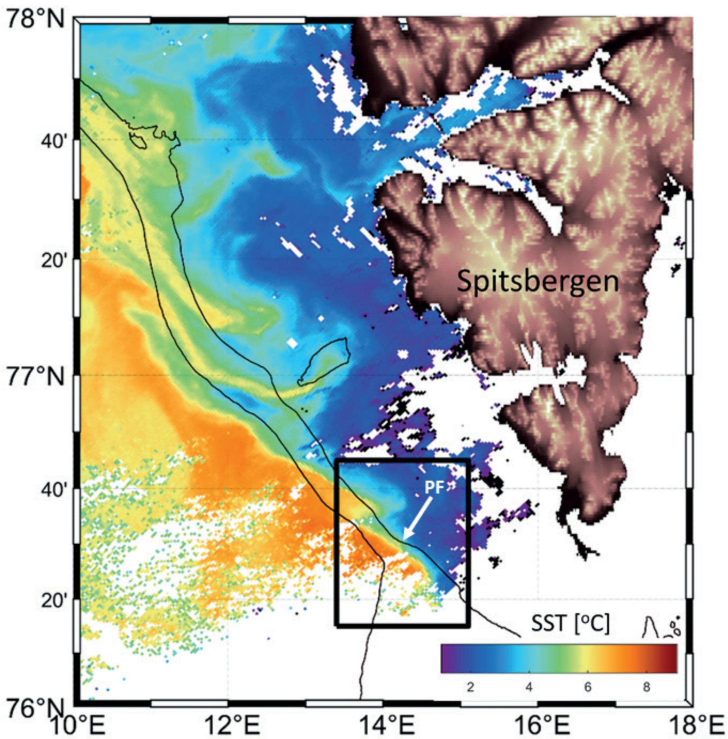

Fig. 2 - Visible infrared imaging radiometer suite satellite image of the sea surface temperature west of Spitsbergen on 30 September 2019 at 09:31 UTC. Clouds are masked in white. The area of study (rectangle) is centred on the PF, separating warmer surface waters to the SW from colder surface waters to the NE. The 300 and 1,000 m isobaths are shown with black curves.

Padman and Erofeeva, 2004; Kowalik and Marchenko, 2023). Diurnal currents are predominantly barotropic (uniform with depth), while semidiurnal currents exhibit a more complex structure in the water column (Kasajima and Svendsen, 2002). Cross-shelf tidal currents near the PF can contribute to mixing between the AW and ArW, which must be considered when calculating northward heat and salt transport or conducting numerical model simulations.

In September–October 2019, the Environmental Knowledge and Operational Effectiveness (EKOE) programme of the North Atlantic Treaty Organisation (NATO) Science and Technology Organisation (STO) Centre for Maritime Research and Experimentation (CMRE) participated in the NARVAL19 sea trial, led by the French Naval Hydrographic and Oceanographic Service (SHOM) on board the French research vessel *Pourquoi pas?* (Poulain *et al.*, 2019). The primary scientific activities took place near the shelf break and slope SW of Spitsbergen, as shown in Figs. 1 and 2. This region was selected due to the dominance of the eastern WSC and the PF, where deep flow measurements (Bensi *et al.*, 2019) have detected anomalies linked to topographically trapped waves induced by atmospheric forcing. These anomalies enhance mixing between upper and deep layers on the Spitsbergen continental slope, gradually warming and salinising the deep water (Bensi *et al.*, 2019). The SST satellite image (Fig. 2) illustrates that the surface PF during the sea trial largely followed the shelf break, exhibiting some meandering and filaments that occasionally extended onto the shelf north of the study area.

This study aims to assess the variability of currents and thermohaline properties near the shelf break SW of Spitsbergen, focusing on temporal scales between 12 hours and a few days and spatial scales from 0.5 to 15 km, using NARVAL19 *in situ* data. Special attention is given to tidal currents and the spatio-temporal distribution of thermohaline properties. Details on the oceanographic data and analysis methods are provided in Section 2. Results are presented in Section 3, followed by a discussion in Section 4 and concluding remarks in Section 5.

2. Data and methods

2.1. Moorings

During the NARVAL2019 cruise, oceanographic moorings were deployed to provide fixed-point time series of measurements, enabling a detailed characterisation of the vertical structure and dynamics of the water column. These moorings were strategically positioned near the shelf break SW of Spitsbergen at six stations, forming a 30 km×15 km rectangle aligned with the bathymetry. In particular, CMRE1, CMRE4, and SHOM2 were deployed in deeper waters (~700 m) on the slope, while CMRE2, SHOM3, and CMRE3 were placed on the shelf (~200 m), as shown in Fig. 3. This configuration was designed to capture both cross-shelf and along-shelf dynamics. The mooring array was located inshore of the S1 mooring discussed in Bensi *et al.* (2019).

The moorings were equipped with four types of oceanographic sensors: 1) Sea-Bird SBE-37 and SBE-39 sensors for temperature and salinity measurements; 2) RBR TDR-2050P loggers for temperature and pressure recording; 3) acoustic Doppler current profilers (ADCPs) – Teledyne RDI Quartermaster 150 kHz, Sentinel V 300 kHz, and Nortek Continental 190 kHz, all upward looking, for profiling water column currents; 4) Nortek Aquadopp 6000 (2 MHz) acoustic current meters (ACMs) for measuring currents at specific depths. Table 1 provides further details on the moorings, including the sampling periods and the nominal depths of the ADCPs and ACMs.

Table 1 - Details on the oceanographic moorings deployed on the shelf break SW of Spitsbergen.

Mooring	Water depth	Coordinates (Lat, Lon)	Dates (deployment, recovery)	Oceanographic instruments	Depth range of processed data, sampling period
CMRE1	704 m	76.5828° N, 13.7313° E	22 September 16:00 UTC, 7 October 13:00 UTC	Acoustic Doppler current profiler (ADCP) 150 kHz (cell size 8 m, nominal depth 250 m), SBE-37s, RBRs	80–240 m, ADCP: 5 min, SBE-37: 5 min, RBR: 10 s
CMRE2	217 m	76.6693° N, 14.1057° E	22 September 16:00 UTC, 7 October 11:00 UTC	ADCP 300 kHz (cell size 4 m, sensor depth 150 m), SBE-37s, RBRs	80–140 m, ADCP: 5 min, SBE-37: 5 min, RBR: 10 s
CMRE3	220 m	76.4706° N, 14.8797° E	26 September 07:31 UTC, 7 October 04:00 UTC	ADCP 300 kHz (cell size 4 m, sensor depth 150 m), SBE-37s, RBRs	80–152 m, ADCP: 5 min, SBE-37: 5 min, RBR: 10 s
CMRE4	717 m	76.3767° N, 14.4603° E	26 September 17:45 UTC, 9 October 06:30 UTC	ADCP 150 kHz (cell size 8 m, sensor depth 250 m), SBE-37s, RBRs	48–244 m, ADCP: 5 min, SBE-37: 5 min, RBR: 10 s
SHOM2	702 m	76.4817° N, 14.1392° E	22 September 04:48 UTC, 7 October 06:29 UTC	ADCP 400 kHz (cell size 4 m, sensor depth 46±2 m), ACM 2 MHz (nominal depths 125, 200, 350, and 500 m), SBE-39s	ADCP: 9–37 m, 5 min; ACM: 128, 207, 355, 509 m, 1 min, SBE-39: 30 s
SHOM3	143 m	76.5745° N, 14.5218° E	22 September 06:28 UTC, 7 October 10:53 UTC	ADCP 190 kHz (cell size 4 m, sensor on bottom), SBE-39	ADCP: 20–132 m, 2.5 min, SBE-39: 30 s
WW	238 m	76.5122° N, 14.2692° E	27 September 07:52 UTC, 29 September 08:41 UTC	SBE-49 CTD, SBE-43 DO, Wetlabs ECOpuck BB2F	4–203 m, 0.125 s

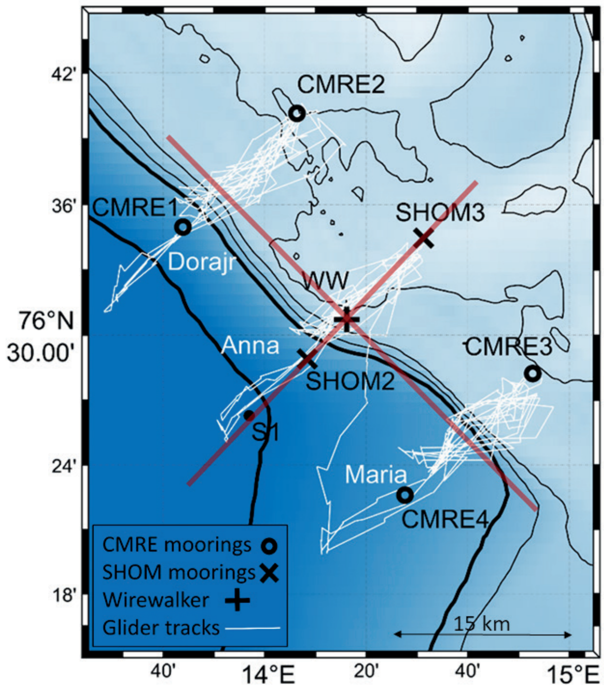

Fig. 3 - Bathymetry of the area of study on the shelf break SW of Spitsbergen with the locations of the moorings (CMRE1, CMRE2, CMRE3, CMRE4, SHOM2, and SHOM3) and the Wirewalker. The tracks of gliders Maria, Anna, and Dora Jr. are shown with white curves. Isobaths are at 100, 200, 300, and 400 m (thin lines), and at 500 and 1,000 m (thick lines). The location of mooring S1 is also shown for reference. The cross- and along-shelf coordinate system is represented by straight red lines. It is rotated CCW by 45° with respect to the E-N system.

For three moorings (CMRE1, CMRE2, and CMRE3), the ADCP range was affected by significant variations, likely due to reflections from vertically migrating zooplankton (descending during daylight and ascending at night) and mooring line inclinations caused by strong currents [with maximum tilt angles of ~25°, resulting in depth variations of ±20 m; see Poulain *et al.* (2020)]. Unlike Poulain *et al.* (2020), this study considers extended depth ranges, including limited intermittent data gaps (< 30%, see Table 1). Additionally, the ADCP horizontal velocities are corrected for an 8.5° magnetic declination.

2.2. Wirewalker profiler

A Wirewalker (WW) profiler, manufactured by Del Mar Oceanographic, was deployed on a mooring near the shelf break in the centre of the study area (see Fig. 3) to monitor the upper water column down to ~200 m with high-frequency sampling. The WW moves along a wire, descending under the propulsion of surface wave motion and ascending by its own positive buoyancy (Rainville and Pinkel, 2001; Pinkel *et al.*, 2011; Poulain *et al.*, 2019).

Between 27 and 29 September 2019, the WW completed 178 profiles in ~2 days, with an average interval of 17 minutes between consecutive ascents. It was equipped with an SBE-49 conductivity-temperature-depth (CTD) sensor, an SBE-43 dissolved oxygen sensor, and a Wetlabs ECOpuck BB2F sensor to measure chlorophyll, coloured dissolved organic matter, and particle backscatter. The CTD took samples at 8 Hz, with a mean upward velocity of 0.7 m/s, which corresponds to a vertical resolution of ~10 cm.

2.3. Gliders

During the NARVAL19 cruise, three Teledyne Webb Research Slocum gliders were deployed and operated between 22 September and 5 October 2019. Two of them, Dora Jr. and Maria, were

G2 deep Slocum models equipped with a pumped SBE CTD and Wetlabs EcoPuck sensors. The third glider, Anna, was a G3 deep Slocum equipped with rechargeable batteries and a pumped SBE CTD. All sensors had a sampling period of 6 s.

The gliders were piloted to conduct synchronised back-and-forth transects across the shelf, connecting specific moorings (see Fig. 3 for tracks): Dora Jr. navigated between CMRE1 and CMRE2, Anna between SHOM3, WW, and SHOM2, and Maria between CMRE4 and CMRE3. Each transect, approximately 24 km long, lasted around 12 hours and was performed continuously throughout the experiment. The gliders operated at depths of up to 300 m, with a typical horizontal resolution of ~0.5 km at mid-depth. On the shelf, they adjusted their dive profiles to maintain a distance of 20–30 m from the seafloor, which increased the horizontal resolution to 0.2 km. The first four transects extended further offshore and took about a day to complete. In total, each glider performed 19 transects in 12.4 days, from 22 September at 07:29 UTC to 4 October at 21:25 UTC.

2.4. Drifters

Satellite-tracked drifters from the Global Drifter Program were deployed in the study area to measure near-surface currents, SST, and atmospheric pressure (Niiler, 2001; Lumpkin and Pazos, 2007). These drifters, known as surface velocity program barometer (SVPB) units, consist of a spherical surface buoy attached to a weighted nylon drogue which enables them to track horizontal currents at a nominal depth of 15 m. Each surface buoy is equipped with alkaline batteries, an Iridium satellite transmitter, a thermistor for measuring surface temperature, and a barometer for monitoring sea level pressure. Data are collected and transmitted hourly.

A total of 24 drifters were deployed along three transects crossing the shelf break on 26, 27, and 29 September 2019. Deployment locations are shown in Fig. 4, along with the drifter trajectories until 7 October 2019 at 04:00 UTC. It is noteworthy that looping patterns are widespread in the drifter tracks, especially in the south-eastern corner of the study area.

2.5. Analysis methods

The temperature, salinity, pressure, and current data collected from moorings, gliders, and the WW underwent automated outlier removal using climatological thresholds and were, then, subjected to a manual quality check. Conservative temperature and absolute salinity were calculated (Feistel, 2012), along with potential density anomaly and spiciness relative to a reference pressure of 0 dbar (McDougall and Krzysik, 2015). Spiciness is particularly useful because the PF can be quasi-density-compensated and generally shows a strong spiciness signature separating warmer, saltier (i.e. spicier) waters from colder, fresher waters.

For the WW data, temperature, salinity, and density were binned with a vertical resolution of 0.5 m, considering only upcasts. A bi-linear interpolation in depth (0.5 m) and time (15 minutes) was applied, over a vertical range of 4–203 m.

Vertical isopycnal displacements were estimated relative to a three-day moving mean (Poulain *et al.*, 2023; Poulain, 2024). High-frequency displacements of isotherms, isohalines, and isopycnals were assumed to result from vertical water movement rather than horizontal advection, as the vertical gradients of water properties are generally steeper than the horizontal ones.

A bandpass filter was applied to the WW ADCP and drifter data to extract the diurnal and semidiurnal tidal signals: a second-order Butterworth filter with cutoff periods of 10–26, 10–14, or 22–26 hours was applied twice, forwards and backwards, to prevent phase distortion.

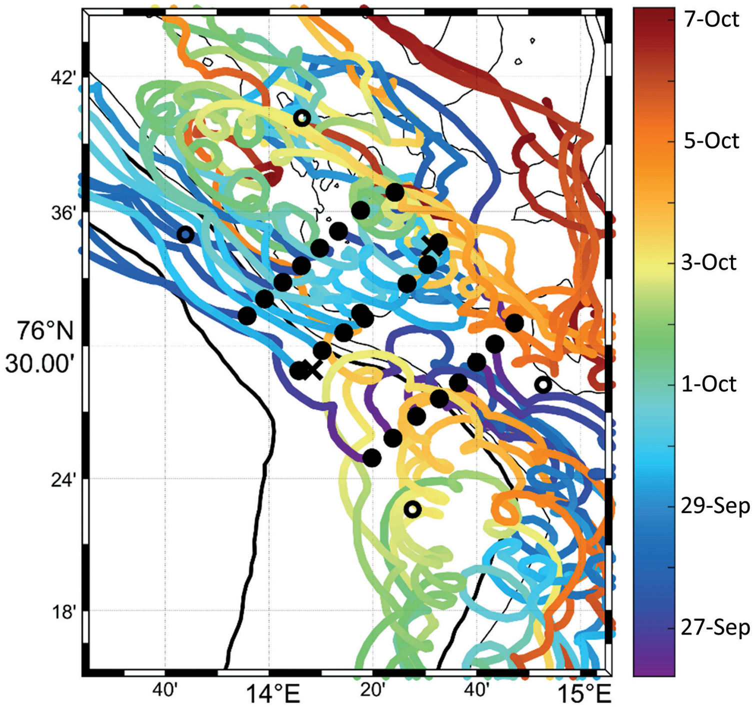

Fig. 4 - Initial positions (black dots) and tracks (until 7 October 2019 at 04:00 UTC) of the 24 SVPB drifters deployed during NARVAL19. The tracks are colour-coded according to time. Some isobaths (black curves) and mooring locations (black crosses and circles) are also shown for reference.

Pressure anomalies at ~200 m depth were estimated using the hydrostatic equation with g = 9.80665 m/s² and WW-measured density profiles.

The ADCP data were linearly interpolated to uniformly distributed depths with vertical resolution of 4 m. The processed sampling period was 5 minutes, except for SHOM3 (2.5 minutes). To ensure that the harmonic analysis focused on simultaneous data acquisitions, the time period was limited to 10.46 days (26 September 2019, 17:00 UTC – 7 October 2019, 04:00 UTC). This is shorter than the 14.79-day beat period of the principal lunar (M2) and solar (S2) semidiurnal tides, resulting in slightly overestimated tidal amplitudes (see Appendix for more details).

Mean flow and velocity standard deviation ellipses (Yuill, 1971) were calculated from moored ADCP and drifter velocity data.

SVPB drifter velocities were grouped into circular bins with a radius of 10 km, centred on the six moorings. For each bin, simultaneous drifter velocities were averaged. The resulting time series were, then, sorted chronologically, and any data gaps were filled by linear interpolation.

A standard harmonic analysis using the t_tide algorithm (Pawlowicz *et al.*, 2002) was applied to ADCP currents, temperature, salinity, density, vertical isopycnal displacements, and drifter velocities. Up to four tidal constituents were used: principal lunar semidiurnal (M2, 12.42 hours), principal solar semidiurnal (S2, 12 hours), lunisolar diurnal (K1, 23.93 hours), and lunar diurnal (O1, 25.82 hours). The error bars were estimated using bootstrap confidence intervals based on white noise. Potential contamination of semidiurnal signals by inertial motions is likely due to the small frequency difference between the local inertial frequency (0.5142 cpd) and the M2 tidal frequency (0.5175 cpd). These frequencies cannot be reliably separated in time series less than, or equal to, 10 days, according to the Rayleigh criterion.

3. Results

3.1. Sea level variations at the mooring sites

The pressure data from the deepest instruments on the moorings were first analysed to investigate the variability of the sea level due to the tides. The pressure measurements were converted to depth using the hydrostatic equilibrium equation. Harmonic analysis was performed over the common observation period, and a bandpass-filter was applied to the time series to isolate semidiurnal and diurnal frequency components.

As a first approximation, we assumed minimum vertical displacement of the deepest sensors due to mooring motion induced by strong currents and neglected the effect of internal tides, which are limited to ~1 cm (see Section 3.4 and Fig. 15c). Under this assumption, the bandpass-filtered depths can be interpreted as representing tidally induced sea level variations. The filtered time series are presented in Fig. 5, while the results of the harmonic analysis are summarised in Table 2. The error bars for the amplitudes and phases are less than 1 cm and 4°, respectively.

The semidiurnal tidal constituents, M2 and S2, are dominant, with amplitudes ranging from 55 to 84 cm and 20 to 34 cm, respectively. In contrast, the diurnal constituents are generally weaker, especially on the shelf, with amplitudes below 15 cm, except at mooring CMRE4, where the K1 constituent reaches 33 cm. The slight phase increase from CMRE3 to CMRE2 on the shelf and from CMRE4 to CMRE1 on the slope (Table 2) suggests a NW-ward along-shore propagation of the M2 tide.

Table 2 - Results of the harmonic analysis (amplitudes and phases) applied to the sea level height at the mooring sites for the period from 26 September 2019 at 17:00 UTC to 7 October 2019 at 04:00 UTC. Error bars on the amplitudes and phases are bounded by 1 cm and 4°, respectively.

Mooring	O1		K1		M2		S2	
	Amp. [m]	Phase [°]	Amp. [m]	Phase [°]	Amp. [m]	Phase [°]	Amp. [m]	Phase [°]
CMRE1	0.15	163	0.13	19	0.80	352	0.22	11
CMRE2	0.04	54	0.04	212	0.56	352	0.21	14
CMRE3	0.03	52	0.04	230	0.55	349	0.21	11
CMRE4	0.11	151	0.33	28	0.55	345	0.21	39
SHOM2	0.10	86	0.13	287	0.84	355	0.34	351
SHOM3	0.05	97	0.09	247	0.58	347	0.20	8

The bandpass-filtered time series (Fig. 5) clearly reveal a fortnightly tidal cycle, with maximum tidal heights occurring between 28 September and 1 October, corresponding to the spring tide. Interestingly, the New Moon during this period was on 28 September.

3.2. Tidal currents at the mooring sites

The results of the harmonic analysis applied to the mooring ADCP data, which only considers the K1 and M2 tidal constituents, are illustrated in Figs. 6 to 10.

At mooring CMRE1 (Fig. 6), the mean currents are relatively uniform with depth, with a zonal component of -13 ± 6 cm/s and a meridional component of 20 ± 8 cm/s. The tidal model explains up to 25% of the total variance at 132 m depth. The M2 and K1 semi-major axes have comparable

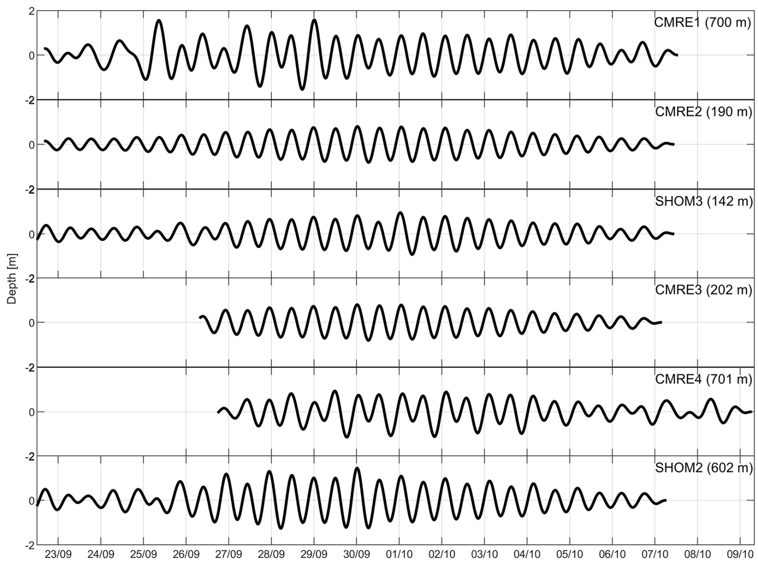

Fig. 5 - Bandpass-filtered (10–26 h) depth anomaly of deep sensors on all the moorings versus time. The mean depth for each mooring is indicated in the upper right corner of each subplot.

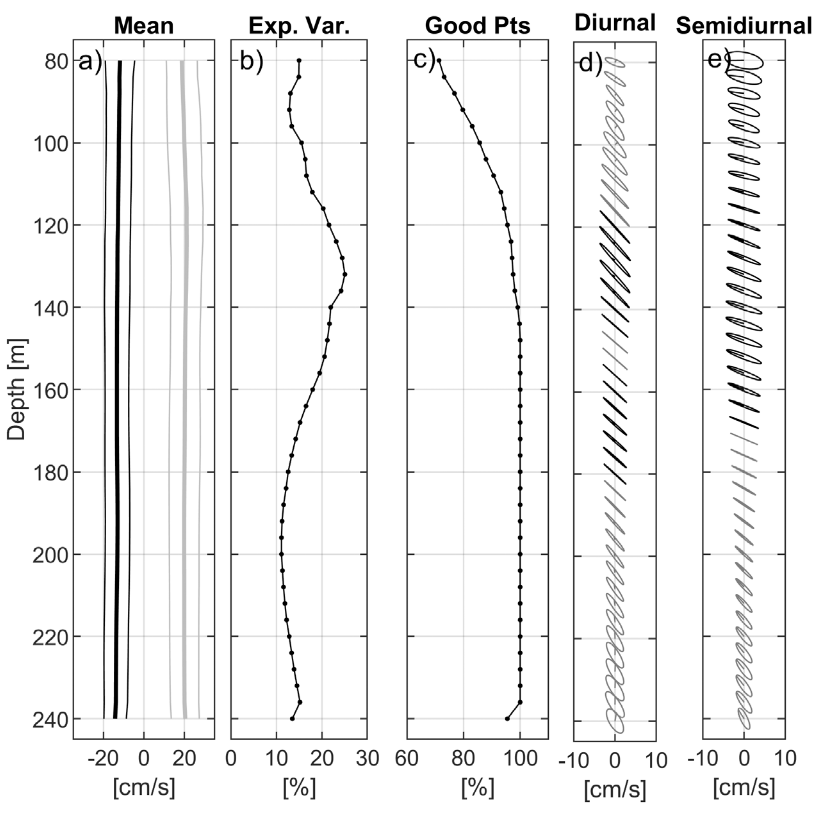

Fig. 6 - Zonal (black) and meridional (grey) components of mean flow (thick) ± velocity standard deviation (thin) versus depth for mooring CMRE1 (a). Explained variance of the tidal model (b) and percentage of good data (c). Tidal ellipses for the K1 (d) and M2 (e) constituents versus depth: CW and CCW rotations are shown in black and grey, respectively. A line in the ellipse indicates the Greenwich phase.

amplitudes (3–5 cm/s), while the semi-minor axes remain limited to ~1 cm/s. The tidal ellipses are mainly oriented in a NW-SE direction. Diurnal ellipses are generally counterclockwise (CCW), while semidiurnal motions in the upper water column (down to ~170 m) exhibit clockwise (CW) rotation and CCW rotation below.

At mooring CMRE2, located on the Spitsbergen shelf (Fig. 7), the mean current near the bottom (140 m depth) is nearly zero and gradually increases to ~8 cm/s in the SE direction at 80 m depth. The standard deviation varies between 8 and 13 cm/s. The tidal model accounts for up to 17% of the total variance at 80 m depth. The K1 tidal ellipses are relatively uniform throughout the water column, with semi-major axes ranging from 5 to 7 cm/s, semi-minor axes near 1 cm/s, CW rotation, and an inclination in the NW-SE direction. Between 80 and 100 m, the M2 tidal ellipses have semi-major axes up to 7 cm/s, semi-minor axes up to 2 cm/s, CW rotation, and an inclination in the NE-SW direction. Below 100 m, M2 tidal currents become almost rectilinear, with amplitudes of 4–5 cm/s, predominantly aligned along the zonal direction.

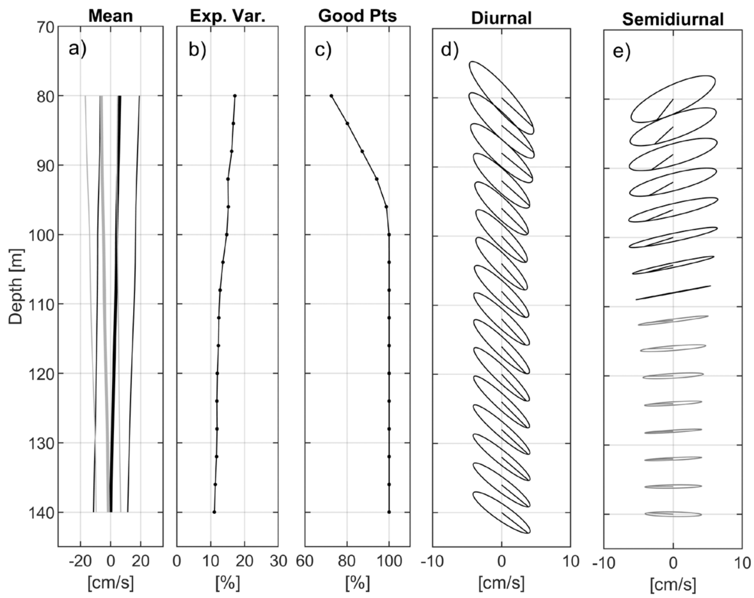

Fig. 7 - Zonal (black) and meridional (grey) components of mean flow (thick) ± velocity standard deviation (thin) versus depth for mooring CMRE2 (a). Explained variance of the tidal model (b) and percentage of good data (c). Tidal ellipses for the K1 (d) and M2 (e) constituents versus depth: CW and CCW rotations are shown in black and grey, respectively. A line in the ellipse indicates the Greenwich phase.

At CMRE3 (Fig. 8), the mean current is weak near the bottom (< 2 cm/s at 150 m depth) and increases to ~13 cm/s in the SE direction at 80 m depth. The standard deviation ranges from 10 to 16 cm/s, with the tidal model explaining 56–63% of the variance. The K1 ellipses remain fairly consistent with depth, with semi-major axes of 11–14 cm/s, semi-minor axes of 6–8 cm/s, CW rotation and a NW-SE inclination. The M2 constituent shows semi-major (semi-minor) axes between 9 (1) cm/s at 150 m and 16 (7) cm/s at 80 m, with all tidal currents rotating CW.

At mooring CMRE4 (Fig. 9), the mean current is predominantly northwards, with the zonal component below 2 cm/s and the meridional component between 10 and 12 cm/s. The standard deviation ranges from 7 to 13 cm/s, and the tidal currents explain up to 61% of the total variance. The K1 semi-major axis increases with depth, from ~4 cm/s at 60 m to ~7 cm/s at 240 m, while the

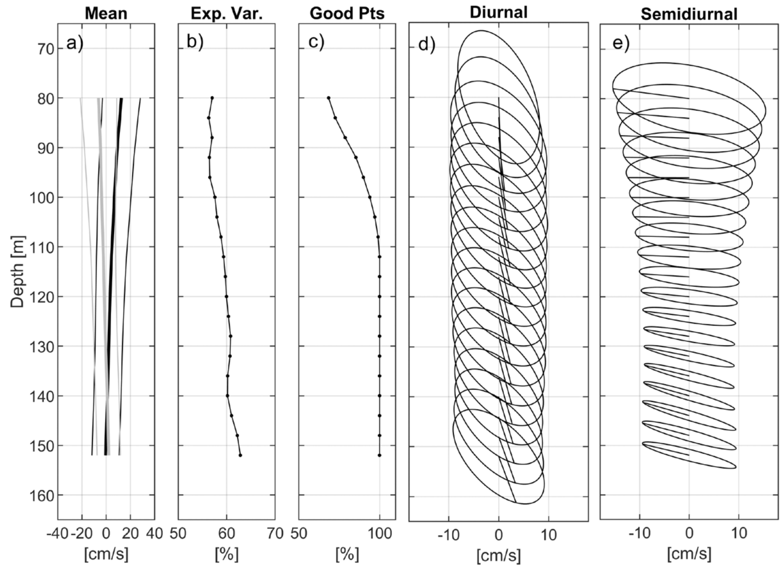

Fig. 8 - Zonal (black) and meridional (grey) components of mean flow (thick) ± velocity standard deviation (thin) versus depth for mooring CMRE3 (a). Explained variance of the tidal model (b) and percentage of good data (c). Tidal ellipses for the K1 (d) and M2 (e) constituents versus depth: CW and CCW rotations are shown in black and grey, respectively. A line in the ellipse indicates the Greenwich phase.

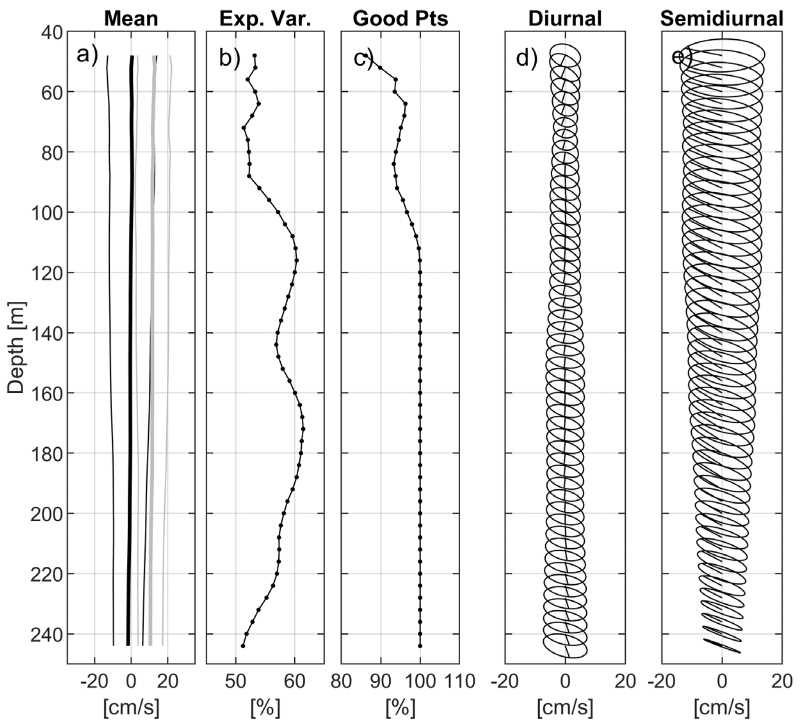

Fig. 9 - Zonal (black) and meridional (grey) components of mean flow (thick) ± velocity standard deviation (thin) versus depth for mooring CMRE4 (a). Explained variance of the tidal model (b) and percentage of good data (c). Tidal ellipses for the K1 (d) and M2 (e) constituents versus depth: CW and CCW rotations are shown in black and grey, respectively. A line in the ellipse indicates the Greenwich phase.

semi-minor axes remains between 3 and 4 cm/s. In contrast, the M2 semi-major axis decreases with depth, from 14 to 6 cm/s, and the semi-minor axis decreases from 6 cm/s to almost 0 cm/s. Both constituents exhibit CW rotation and a NW-SE inclination.

At SHOM3 (Fig. 10), the mean current varies between -1 and 8 cm/s zonally and -8 to 4 cm/s meridionally. Above 120 m depth, the flow is predominantly directed SE-wards. The tidal model accounts for up to 42% of the total variability at 120 m. The K1 ellipses are oriented NW-SE, with decreasing eccentricity with depth. The semi-major axis ranges from 6 to 10 cm/s, while the semi-minor axis varies from 3 to 8 cm/s, with CW rotation. The M2 ellipses exhibit significant depth-dependent variability. In the upper layers, they are oriented NE-SW, with a semi-major axis reaching 11 cm/s. Below 100 m, the orientation shifts to NW-SE, and the semi-major axis drops to ~7 cm/s. The rotation shifts to CCW, but this change is minor, as the motion is nearly rectilinear.

The vertical structure of the tidal currents at SHOM2 is not discussed in detail due to the limited observations, which cover only shallow depths (9 to 37 m), with four additional selected depths down to 509 m.

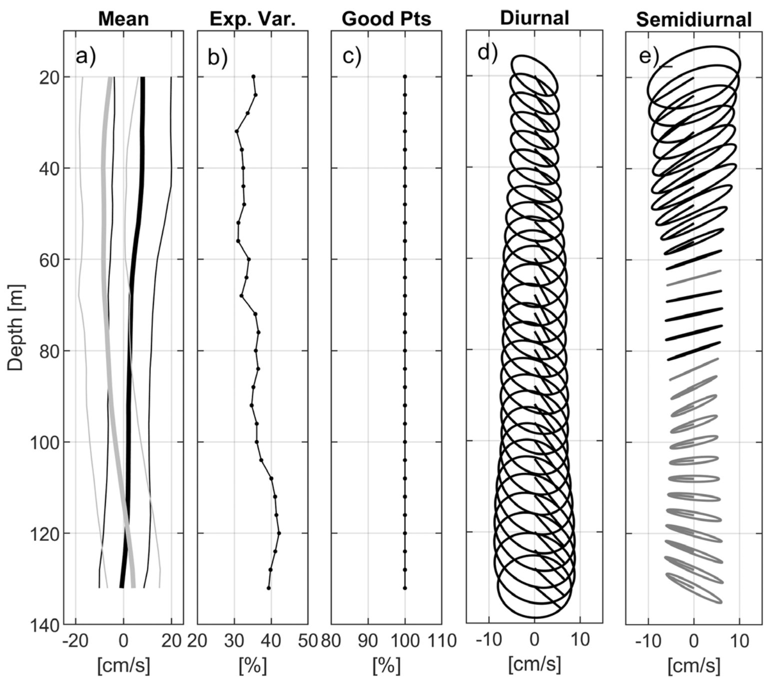

Fig.10 - Zonal (black) and meridional (grey) components of mean flow (thick) ± velocity standard deviation (thin) versus depth for mooring SHOM3 (a). Explained variance of the tidal model (b) and percentage of good data (c). Tidal ellipses for the K1 (d) and M2 (e) constituents versus depth: CW and CCW rotations are shown in black and grey, respectively. A line in the ellipse indicates the Greenwich phase.

3.3. Horizontal structure of the currents near 128 m and 15 m depths

The currents at a depth close to 128 m, where all moorings provided reliable ADCP data, are now examined and the results with those obtained with the drifters near 15 m depth are compared. Fig. 11a shows the mean flow and velocity standard deviation ellipses, along with the standard deviation ellipses of the reconstructed tidal currents (considering only the M2 and K1

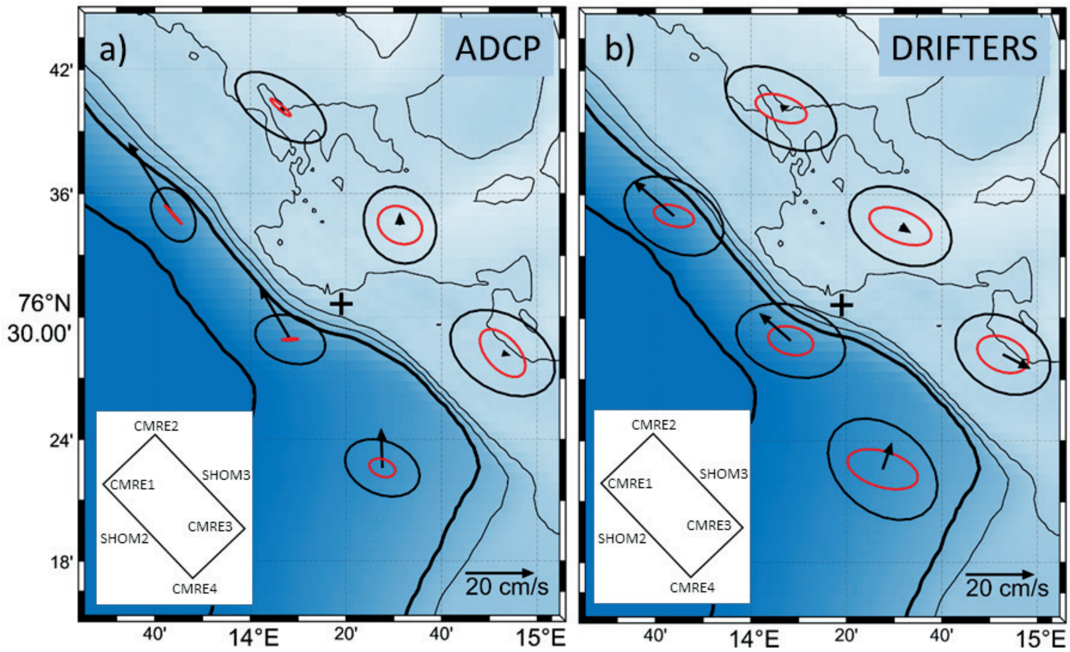

Fig. 11 - Mean flow (arrows) and velocity standard deviational ellipses (black) near 128 m depth as measured by the ADCPs on the six moorings (a) and near 15 m depth as measured by the SVPB drifters near the six moorings (b). The standard deviation ellipse of the reconstructed tidal currents (M2 + K1) is shown in red.

constituents derived from the harmonic analysis). The corresponding statistics are summarised in Table 3.

The mean currents on the shelf are generally weak, remaining below 4 cm/s. In contrast, the currents on the continental slope strengthen and reach up to 25 cm/s at CMRE1 (see Table 3), with a predominant northward to NW-ward direction. These stronger currents correspond to the eastern branch of the WSC, which follows the continental slope.

The standard deviation of velocities is highest on the shelf, particularly at CMRE3, where the ellipse semi-major axis reaches 16 cm/s. A significant part of this variability is attributed to tidal currents.

Table 3 - Statistics of the currents near 128 m for the common time period (26 September 2019 17:00:00 UTC to 7 October 2019 04:00 UTC) calculated with the current meter data: mean flow and velocity standard deviation ellipses, and standard deviation ellipses of the reconstructed tidal currents (considering only the M2 and K1 constituents) derived from the harmonic analysis.

Mooring	Mean U [cm/s]	Mean V [cm/s]	Mean speed [cm/s]	Semi-major axis [cm/s]	Semi-minor axis [cm/s]	Inclination [°]	Semi-major axis K1+M2 [cm/s]	Semi-minor axis K1+M2 [cm/s]	Inclination [°]
CMRE1	-13.1	21.1	24.8	8.3	5.6	121	4.8	1.2	24
CMRE2	1.3	-2.3	2.6	14.6	7.4	147	4.5	1.8	12
CMRE3	2.3	-0.7	2.4	16.3	10.8	150	10.2	5.6	61
CMRE4	-0.4	11.6	11.6	11.3	7.7	157	9.9	7.7	59
SHOM2	8.9	15.4	17.8	10.4	6.7	163	6.5	1.9	30
SHOM3	0.0	3.7	3.7	11.5	9.9	124	8.2	5.2	40

The results of the harmonic analysis are summarised in Table 4, with the K1 and M2 tidal current ellipses illustrated in Figs. 12a and 12b. The tidal currents contribute up to 61% of the velocity variance, particularly at CMRE3, with a consistent CW rotation observed at all moorings.

At CMRE1, CMRE2, and SHOM2, the K1 tidal currents are nearly rectilinear and aligned parallel to the isobaths (Fig. 12a). In contrast, the ellipses at the other moorings exhibit less eccentricity and reach their maximum on the shelf at SHOM3 and CMRE3, where the semi-major axis is up to 14 cm/s. The Greenwich phases suggest a NW-ward propagation of the K1 tide on the shelf.

Table 4 - Results of the harmonic analysis applied to the currents near 128 m (t_tide with common time period of 10.46 days, 26 September 2019 17:00:00 UTC to 7 October 2019 04:00 UTC). Error bars are in parentheses. Positive (negative) minor axes correspond to CCW (CW) rotation.

Mooring	Tidal const.	Semi-major axis [cm/s]	Semi-minor axis [cm/s]	Inclination [°]	Phase [°]	Exp. var. [%]
CMRE1	K1	5.4 (0.7)	-0.4 (0.5)	132 (6)	79 (8)	24
	M2	4.3 (0.6)	-0.5 (0.5)	159 (8)	12 (7)	
CMRE2	K1	5.3 (1.1)	-0.9 (0.5)	139 (6)	170 (13)	12
	M2	4.1 (0.8)	0.2 (0.6)	4 (11)	203 (12)	
CMRE3	K1	11.8 (0.7)	-6.7 (0.5)	132 (5)	137 (5)	61
	M2	9.3 (0.7)	-1.0 (0.6)	170 (4)	12 (4)	
CMRE4	K1	5.4 (0.6)	-3.5 (0.7)	163 (14)	92 (14)	59
	M2	12.7 (0.6)	-6.0 (0.6)	162 (4)	332 (4)	
SHOM2	K1	3.3 (0.7)	-0.3 (0.7)	2 (12)	271 (14)	30
	M2	8.6 (0.7)	-2.5 (0.6)	167 (5)	345 (5)	
SHOM3	K1	9.2 (0.7)	-7.4 (0.8)	154 (17)	160 (17)	41
	M2	6.8 (0.7)	0.6 (0.8)	155 (7)	351 (6)	

For the M2 component (Fig. 12b), the strongest tidal currents are observed at CMRE4, where the semi-major axis reaches ~13 cm/s and the semi-minor axis extends to 6 cm/s. The ellipses show high eccentricity on the shelf at CMRE2, SHOM3, and CMRE3, as well as along the slope at CMRE1.

The velocities of the SVPB drifters were analysed between 26 September 2019 at 17:00 UTC and 7 October 2019 at 04:00 UTC. The same approach used for the ADCP currents at 128 m was conducted with the drifter data: the mean currents and their associated standard deviation ellipses were estimated, and a harmonic analysis using the K1 and M2 constituents was performed. The results are shown in Figs. 11b, 12c, and 12d and in Tables 5 and 6.

Near the deepest moorings on the slope base (CMRE1, SHOM2, and CMRE4), the mean flow at 15 m depth is predominantly aligned with the isobaths, with speeds ranging between 8 and 15 cm/s (Fig. 11b, Table 5). This flow pattern corresponds to the eastern branch of the WSC. On the shelf, the mean flow is weaker and even directed SE-wards at CMRE3, where the speed is ~9 cm/s. All standard deviation ellipses are also aligned along the shelf, with semi-major axes ranging from 15 to 18 cm/s and semi-minor axes between 10 and 12 cm/s. The primary tidal constituents, K1 and M2, account for between 15% (for CMRE1) and 42% (for CMRE3) of the velocity variance.

The diurnal tidal currents at 15 m depth (Fig. 12c) generally decrease with latitude, with a maximum semi-major axis of ~10 cm/s at CMRE4. For the M2 constituent, the semi-major axes

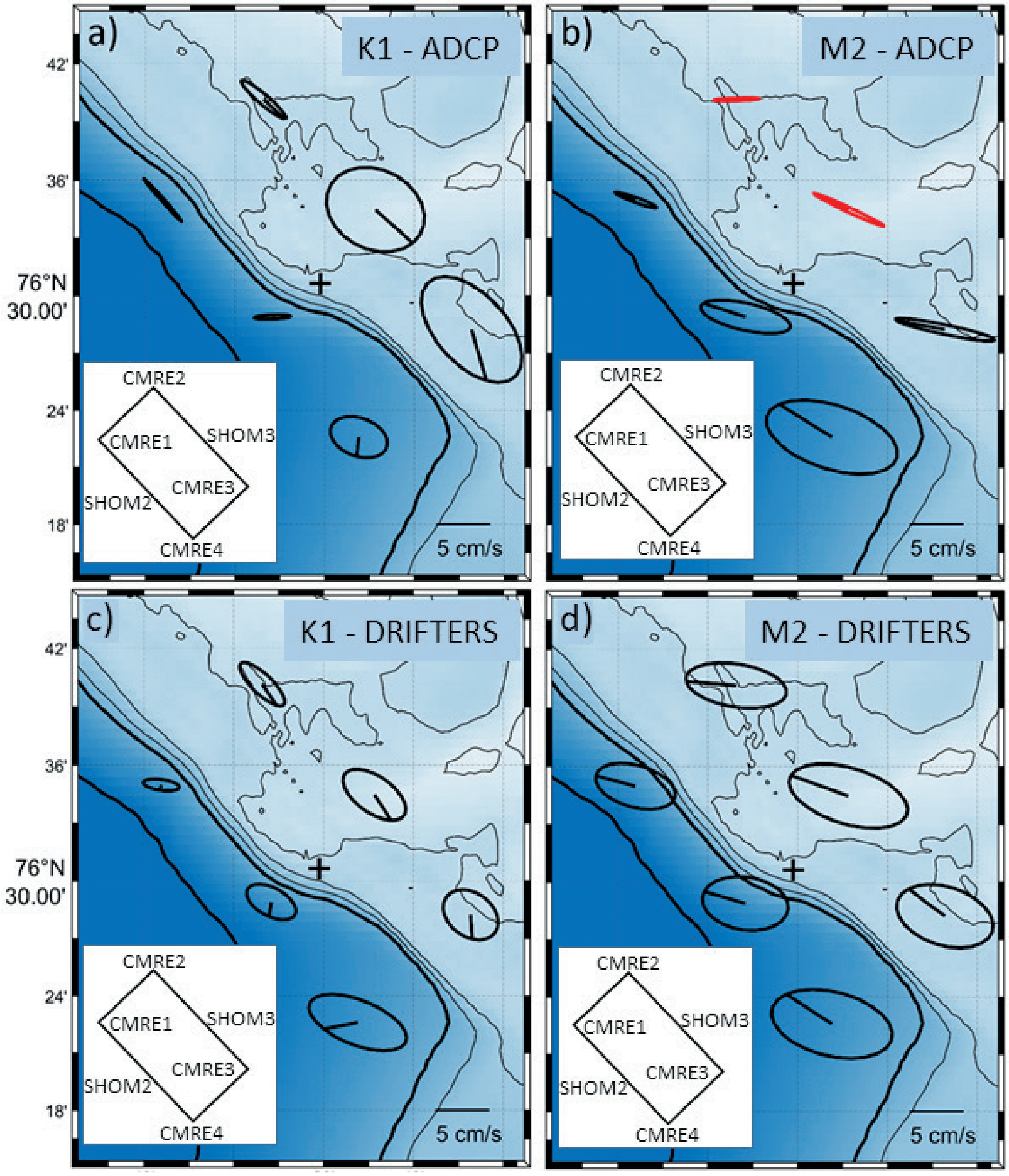

Fig. 12 - Diurnal K1 (a, c) and semidiurnal M2 (b, d) tidal ellipses near 128 m depth as measured by the ADCPs (a, b) on the six moorings and using the drifter velocities at 15 m depth near the six moorings (c, d). The lines in the ellipses indicate the Greenwich phase. Rotation is CW (black) or CCW (red).

are between 8 and 12 cm/s. All tidal currents exhibit a CW rotation. The tidal ellipses are generally aligned with the isobaths, and their eccentricity appears to be less than those estimated from the ADCP data at 128 m depth. For both constituents, the Greenwich phases indicate a NW-ward propagation on the shelf and slope.

Table 5 - Statistics of the currents near 15 m for the common time period (26 September 2019 17:00:00 UTC to 7 October 2019 04:00 UTC) calculated with the drifter data: mean flow and velocity standard deviation ellipses, and standard deviation ellipses of the reconstructed tidal currents (considering only the M2 and K1 constituents) derived from the harmonic analysis.

Mooring	Mean U [cm/s]	Mean V [cm/s]	Mean speed [cm/s]	Semi-major axis [cm/s]	Semi-minor axis [cm/s]	Inclination [°]	Semi-major axis K1+M2 [cm/s]	Semi-minor axis K1+M2 [cm/s]	Inclination [°]
CMRE1	-11.8	10.2	15.6	15.3	9.8	151	5.9	2.9	166
CMRE2	2.5	0.8	2.6	17.2	9.9	151	7.6	3.6	162
CMRE3	8.1	-4.2	9.1	14.6	10.5	150	7.7	4.9	158
CMRE4	2.7	7.8	8.3	17.8	12.5	142	10.6	5.2	163
SHOM2	-9.2	8.0	12.2	16.1	10.1	164	6.6	4.0	166
SHOM3	3.1	-1.9	3.7	15.6	10.2	154	9.4	4.5	159

Table 6 - Results of the harmonic analysis applied to the currents measured by the drifters near 15 m (t_tide with common time period of 10.46 days, 26 September 2019 17:00:00 UTC to 7 October 2019 04:00 UTC). Error bars are in parentheses. Positive (negative) minor axes correspond to CCW (CW) rotation.

Mooring	Tidal const.	Semi-major axis [cm/s]	Semi-minor axis [cm/s]	Inclination [°]	Phase [°]	Exp. var. [%]
CMRE1	K1	3.4 (2.4)	-1.0 (1.6)	172 (28)	86 (44)	15
	M2	7.6 (2.4)	-3.9 (1.5)	164 (19)	1 (26)	
CMRE2	K1	5.5 (2.0)	-1.8 (1.3)	136 (21)	147 (28)	28
	M2	9.3 (1.9)	-4.0 (1.5)	171 (14)	11 (15)	
CMRE3	K1	5.6 1.9)	-4.1 (1.4)	144 (46)	121 (60)	30
	M2	9.3 (2.2)	-5.5 (1.2)	162 (20)	330 (29)	
CMRE4	K1	9.7 (2.3)	-4.2 (1.7)	158 (15)	56 (17)	42
	M2	11.6 (2.1)	-6.0 (2.0)	166 (15)	326 (16)	
SHOM2	K1	5.0 (1.8)	-2.6 (1.3)	152 (29)	100 (38)	30
	M2	8.1 (1.8)	-4.9 (1.3)	171 (18)	348 (25)	
SHOM3	K1	6.7 (2.4)	-3.4 (1.4)	145 (21)	142 (30)	30
	M2	11.3 (2.1)	-5.2 (1.6)	163 (12)	354 (15)	

It is important to note that the error bars associated with the drifter harmonic analysis (Table 6) are generally larger than those from the ADCPs at 128 m (Table 4). In particular, the errors in the inclination of K1 can be substantial, reaching up to 60° for CMRE3. Consequently, the drifter-based estimates should be interpreted with caution. Furthermore, the comparison between the currents at 128 m depth (ADCP) and at 15 m (drifters) is only qualitative, as the depth dependence can be significant (see Figs. 6 to 10).

3.4. Variability of the thermohaline properties

3.4.1. Wirewalker results

The WW provided high-frequency measurements of temperature and salinity profiles over approximately two days (27–29 September 2019) near the centre of the study area (Fig. 3). The observed thermohaline properties are shown as a function of depth and time in Fig. 13.

The conservative temperature reaches a minimum of 3.5 °C at the surface and peaks at 7.4 °C between 10 and 40 m depth. Below this layer, it drops uniformly to 4–5 °C at a depth of 200 m.

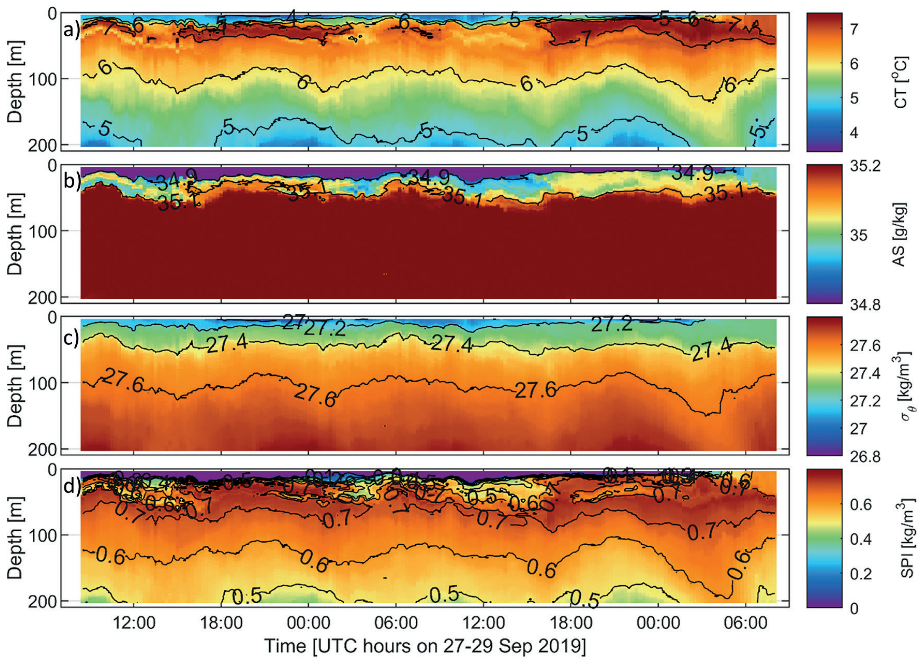

Fig. 13 - Contour plots of conservative temperature (a), absolute salinity (b), potential density anomaly (c) and spiciness (d) measured by the WW, versus depth and time.

The absolute salinity ranges from 33.90 g/kg near the surface to an almost constant 35.19–35.22 g/kg between 80 and 200 m. The potential density anomaly increases with depth from 26.85 to 27.78 kg/m³.

A mixed layer with homogeneous properties forms intermittently near the surface, typically between 10–20 m, deepening to 40–50 m around 06:00 UTC on 29 September. The spiciness follows the temperature trend, with a minimum (~0) at the surface, a maximum of ~0.7 kg/m³ at 40 m depth, and a decrease to 0.4–0.5 kg/m³ at 200 m depth. The thermohaline properties measured by the WW are summarised in the temperature-salinity (T-S) diagram (Fig. 14a). The

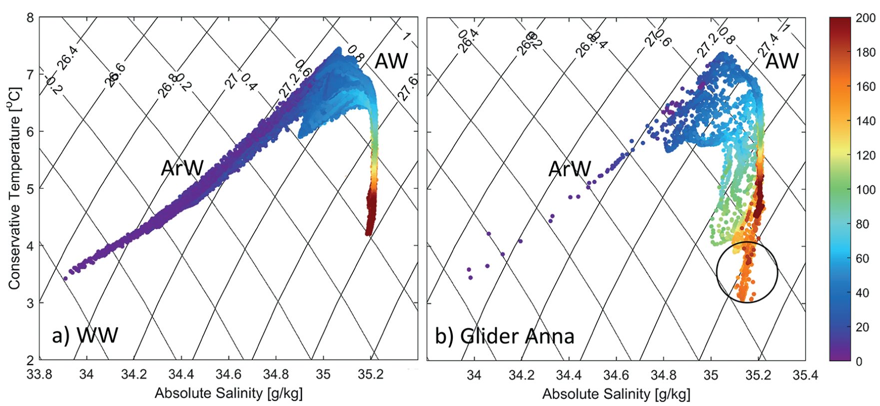

Fig. 14 - T-S diagrams using the WW data (a) and the data of glider Anna during transect no. 9 (b). Points are colour-coded with depth. Isopycnals and curves of constant spiciness are overlaid. The main water masses, AW and ArW, are indicated. A circle highlights the deep cold and salty water on the shelf.

temporal variations of the PF at the WW location are most pronounced in the upper 10–20 m, where fresher, colder ArW interacts with warmer, saltier AW, which is denser and, most importantly, spicier. Below 80 m, salinity remains nearly constant, while temperature decreases and density increases with depth.

Fig. 13 also reveals a periodic signal with a period of about half a day. To investigate this high-frequency oscillation, the depths of the isopycnals (representing displacement relative to the mean stratification) were estimated. They are shown in Fig. 15a as a function of time and depth. The vertical isopycnal displacements are as large as ~80 m, with strong variations observed on the evening of 28 September and the morning of 29 September, exhibiting a ~12-hour periodicity.

A bandpass filter (10–26 hours) applied to isolate semidiurnal and diurnal signals over the 20–140 m depth range, where data are consistently available, indicates that most of the oscillations correspond to internal tides (Fig. 15b). The pressure anomaly near 203 m depth, due to the density variations in the water column above this level (Fig. 15c), is limited to 1 cm.

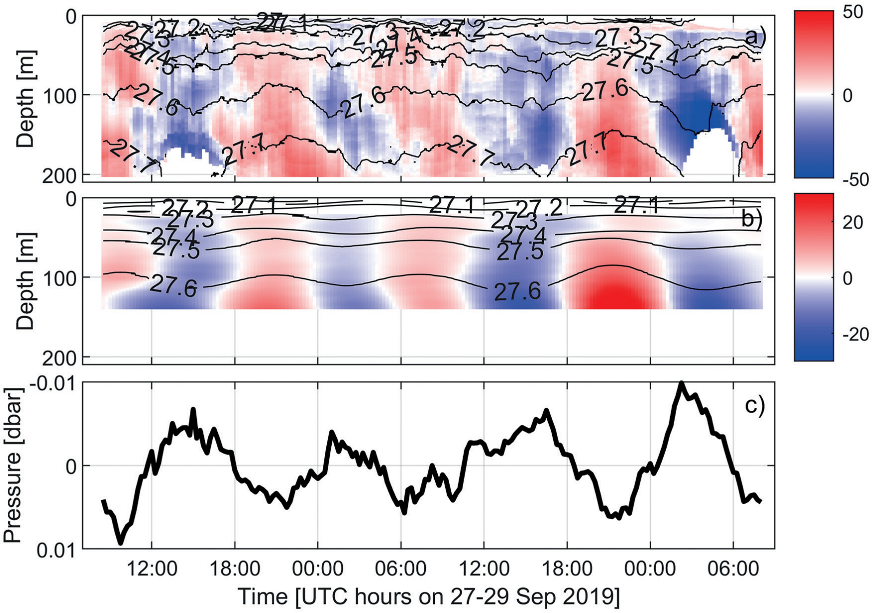

Fig. 15 - Depth of selected isopycnals (black contour lines with 0.1 kg/m^3 interval) and vertical displacements of isopycnals (coloured, in m) from WW measurements, versus depth and time: raw (a) and bandpass-filtered (10–26 h) values over restricted depth range (20–140 m; panel b). Pressure anomaly near 203 m depth due to the density variations in the water column (using hydrostatic approximation; panel c).

The harmonic analysis of isopycnals (Fig. 16) shows that the M2 tide dominates, with an amplitude of 22 m at 140 m depth. At this depth, the vertical motion associated with K1 is limited to 5 m, with both constituents together explaining up to 72% of the observed variability. In the upper water column (20–50 m), M2 and K1 have comparable amplitudes of 4–5 m.

3.4.2. Glider results

Three gliders were piloted along transects crossing the shelf in the study area from 22 September to 4 October 2019. The transects were synchronised and lasted about 12 or 24 hours

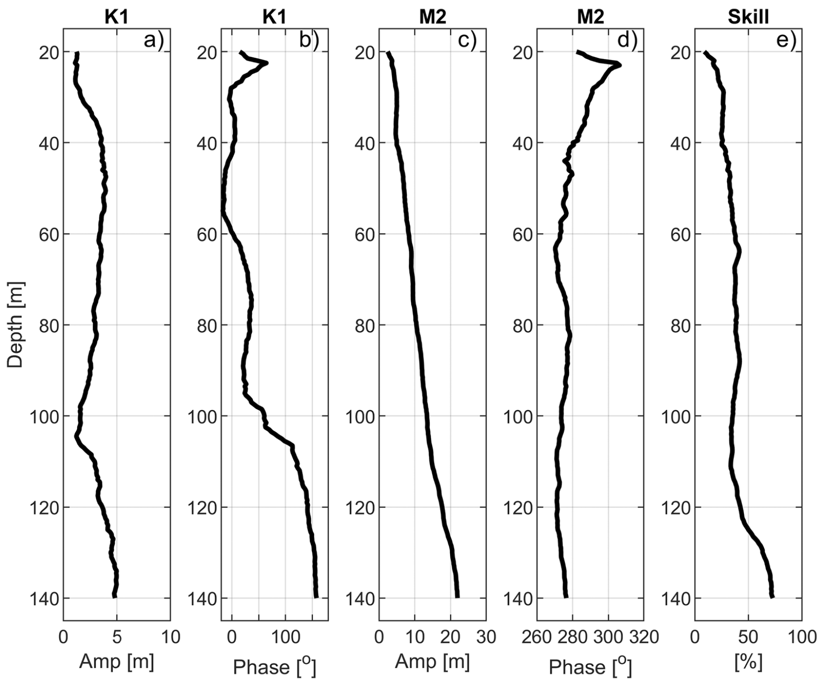

Fig. 16 - Results of the harmonic analysis of the WW vertical isopycnal displacement: amplitude and phase of the K1 (a, b) and M2 (c, d) tidal constituents, and skill or variance explained by the tidal model (e).

each. Examples of glider Anna are shown in Figs. 17 and 18, which show the first 24-hour transect on 22–23 September, and the 12-hour transect no. 9 on 28–29 September contemporaneous with the WW data. These transects, which connect the SHOM3 mooring on the shelf with the

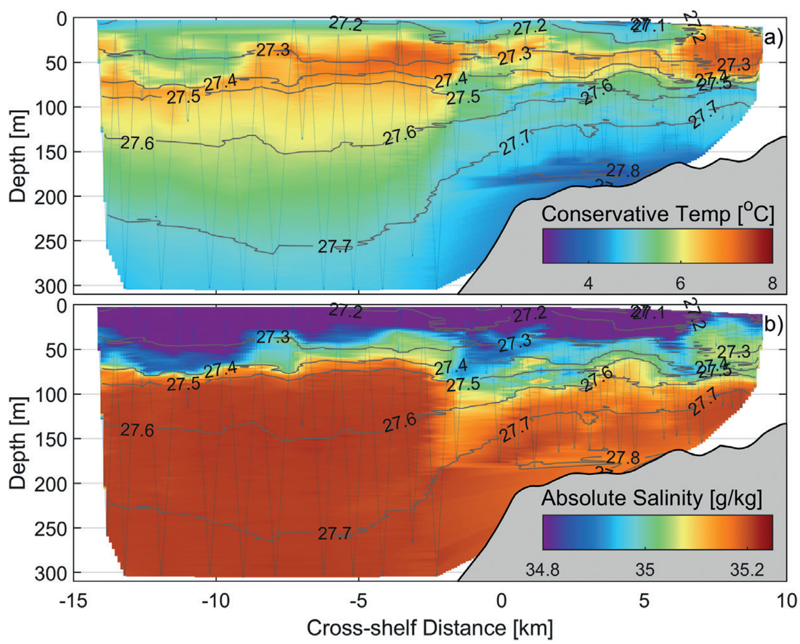

Fig. 17 - Contour plots of conservative temperature (a) and absolute salinity (b) versus depth and cross-shelf distance as measured by glider Anna during 24 hours starting on 22 September 2019 at 07:29 UTC. The depth of selected isopycnals is shown with black contour lines (0.1 kg/m^3 interval). The origin of the cross-shelf distance corresponds to the position of the WW. The depth of the glider is also highlighted with thin lines. The glider moves from right to left.

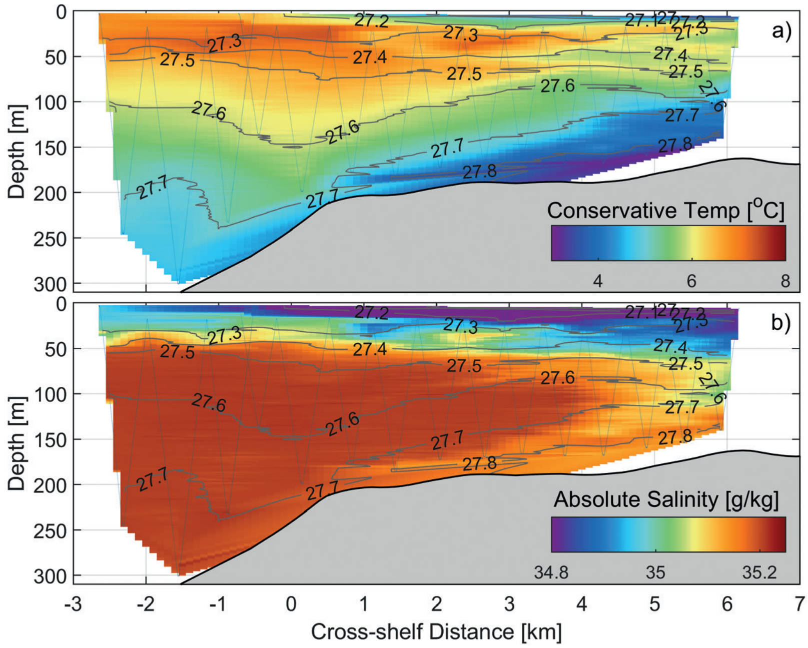

Fig. 18 - Contour plots of conservative temperature (a) and absolute salinity (b) versus depth and cross-shelf distance as measured by glider Anna during 12 hours starting on 28 September 2019 at 20:32 UTC. The depth of selected isopycnals is shown with black contour lines (0.1 kg/m3 interval). The origin of the cross-shelf distance corresponds to the position of the WW. The depth of the glider is also highlighted with thin lines. The glider moves from right to left.

WW and SHOM2, clearly reveal the cold, relatively fresh ArW near the surface, overlaying a layer of warm AW, that extends down to about 100 m. The interleaving of ArW and AW is patchy, leading to meandering isopycnals, some of which are influenced by temporal variability, including the tidal effects observed in the WW data. The coldest water is deeper on the shelf, where the density reaches its maximum, indicating that it is both cold and salty.

The T-S diagram corresponding to the data collected by glider Anna during transect no. 9 is shown in Fig. 14b. In the surface layer down to about 80 m, it is similar to the T-S diagram of the WW (Fig. 14a), although there are fewer observations. Between 80 and 140 m, there is the signature of water with a salinity of 35–35.1 g/kg on the shelf (see Fig. 18). The salty (~35.1 g/kg) and cold (3–4 °C) water, marked with a circle in Fig. 14, corresponds to the water near the shelf bottom mentioned above (onshore from the WW).

A comparison of nearly coincident and collocated data from the WW and glider Anna is presented in Fig. 19, showing the conservative temperature at 100 and 150 m depth. The WW and glider data agree qualitatively, particularly in capturing the temperature rise on 29 September, which is well represented in all the time series. Extrapolation of the tidal model based on the WW data over the entire period of glider operation shows that the local extrema correspond well to the tidal variability observed in the WW temperature records. During the first transect on 22 September, Anna was near WW when the tidal signal was at its lowest. In contrast, during transect no. 9 on 29 September, the glider passed close to WW when the temperature was at its peak. This highlights the need for caution when interpreting transects such as those in Figs. 17 and 18, as temporal variations, primarily driven by internal tides, can lead to artificial spatial variability, particularly in temperature and density.

To investigate the variability of thermohaline properties over space (cross-shelf direction) and time, mean and standard deviation statistics over ~12 days were calculated using glider data at different offshore locations. Due to lack of data, the range of distance across the shelf was reduced to -3 km and 6 km for all gliders. It should be noted that the temporal sampling does not resolve the internal tidal signal, as demonstrated in Fig. 19.

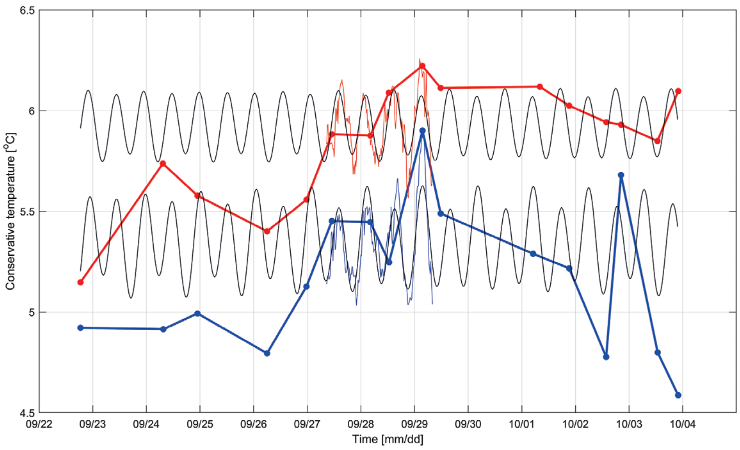

Fig. 19 - Conservative temperature at 100 m (red) and 150 m (blue) depth and zero cross-shelf distance versus time as measured by glider Anna (thick curves) and the WW (thin curves). The tidal model (K1+ M2) based on WW data and extrapolated over the entire period of glider data is overlaid with black curves.

The reduced transects of mean temperature and salinity, together with their standard deviations, are shown in Figs. 20 to 22 for the three gliders. For Anna (Fig. 20), the mean temperature exhibits a near-surface maximum extending offshore, with values above 6.5 °C.

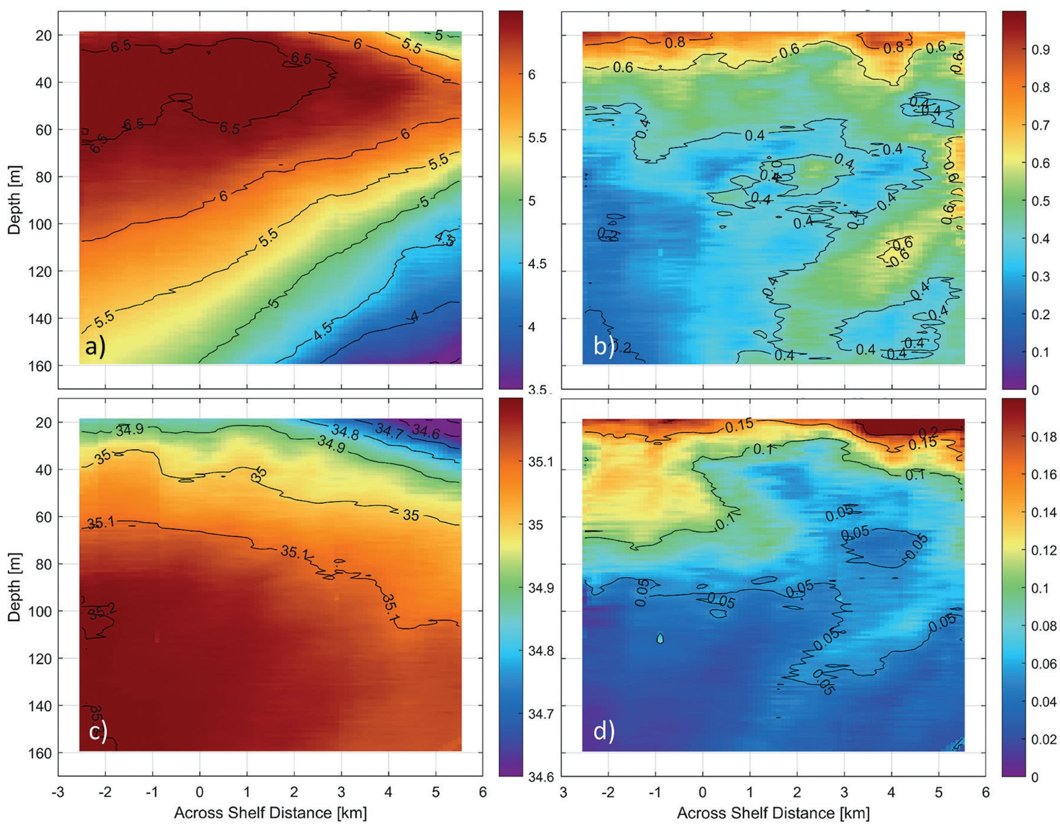

Fig. 20 - Mean conservative temperature (a) and standard deviation (b) versus depth and cross-shelf distance as measured by glider Anna along the transect connecting moorings CMRE1 and CMRE2. Units are in °C. Mean absolute salinity (c) and standard deviation (d) versus depth and cross-shelf distance as measured by glider Anna along the same transect. Units are in g/kg. The depth of selected isotherms and isohalines are shown with black contour lines.

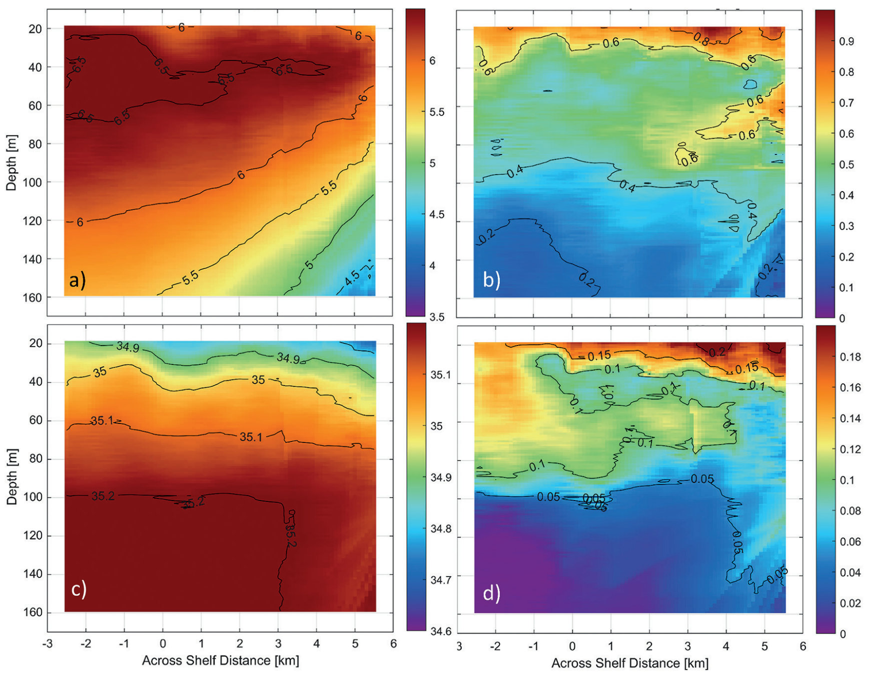

Fig. 21 - Mean conservative temperature (a) and standard deviation (b) versus depth and cross-shelf distance as measured by glider Maria between moorings SHOM2 and SHOM3. Units are in °C. Mean absolute salinity (c) and standard deviation (d) versus depth and cross-shelf distance as measured by glider Anna along the same transect. Units are in g/kg. The depth of selected isotherms and isohalines are shown with black contour lines.

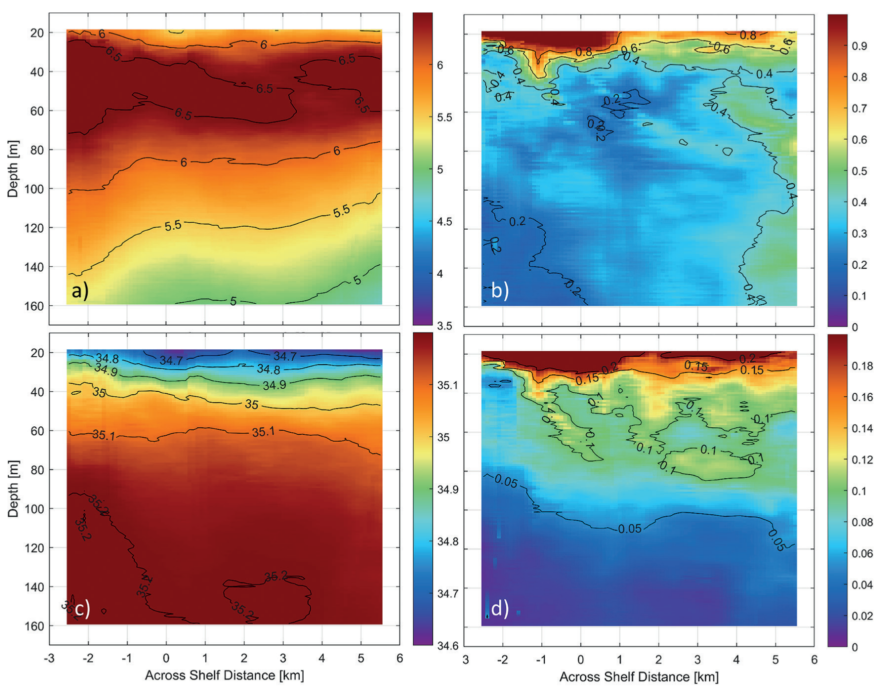

Fig. 22 - Mean conservative temperature (a) and standard deviation (b) versus depth and cross-shelf distance as measured by glider Dora Jr. between moorings CMRE3 and CMRE4. Units are in °C. Mean absolute salinity (c) and standard deviation (d) versus depth and cross-shelf distance as measured by glider Anna along the same transect. Units are in g/kg. The depth of selected isotherms and isohalines are shown with black contour lines.

Cold water occurs both at the surface and at depth on the onshore side. Temperature variability is greatest near the surface (~1 °C) and at mid-depth (60–120 m) onshore, while offshore deep waters show minimal variability (~0.2 °C). Salinity is lowest in the onshore surface layer and increases uniformly with depth. Similar to temperature, the greatest variability in salinity (up to 0.24 g/kg) occurs at the surface, with a secondary maximum (~0.1 g/kg) more offshore near 50 m depth.

The statistical results for glider Maria (Fig. 21), located farther south, are similar to those of Anna, although the cool surface and bottom water is less pronounced onshore. In addition, the mid-depth onshore temperature maximum and the offshore salinity maximum are more pronounced. In contrast, Dora Jr. (Fig. 22) has more distinct thermohaline features. The mean isotherms and isohalines are less inclined, and the near-surface temperature maximum remains near 50 m across the cross-shelf range. The mean salinity increases uniformly with depth, while standard deviations are highest near the surface and decrease with depth and distance from shore.

4. Discussion and conclusions

Currents, thermohaline properties, and sea level were measured with moored and mobile instruments near the shelf break SW of the island of Spitsbergen over periods as long as 15 days in early autumn 2019. Despite the relatively short observation window, these measurements provided new insights into the local oceanography, by capturing variability on time scales between 12 hours to a few days, with a spatial resolution of 0.5 km in the cross-shelf direction and 15 km along the shelf.

The sea level estimated from the deep mooring pressure measurements showed a dominance of semidiurnal tidal constituents, with amplitudes up to 84 cm (Table 2, Fig. 5). On the shelf (at CMRE4), the diurnal tide also played a significant role, reaching 33 cm. A weak NW-ward propagation of M2 along the shelf, which is in qualitative agreement with the numerical simulations of Gjevik *et al.* (1994), Padman and Erofeeva (2004) and Kowalik and Marchenko (2023), was observed. The maximum tidal sea levels occurred between 28 September and 1 October, corresponding to the spring tide.

ADCP measurements at the mooring sites and SVPB drifter data, confirmed the dominance of the eastern branch of the WSC flowing NW-wards along the slope. However, they also revealed weak and mostly SE-ward mean currents on the shelf (Tables 3 and 5, Fig. 11). The highest mean WSC speed (~25 cm/s) was observed at the westernmost mooring (CMRE1), where the continental slope is steeper. This value is consistent with previous drifter estimates (Poulain, 2025).

On the shelf, the variability of the current was largely determined by the tides, with K1 and M2 tidal currents explaining as much as 61% of the velocity variance (see Table 4). The diurnal K1 tidal currents were most pronounced at CMRE3 and SHOM3, with semi-major axis of 9–12 cm/s (Figs. 8, 10, and 12a), while the M2 semi-major axes were between 4 and 9 cm/s (Fig. 12b). On the slope, the M2 currents dominated with a semi-major amplitude near 13 cm/s at CMRE4 (Fig. 12b). The Greenwich phase of the tidal currents (Table 4 and Figs. 12a and 12b) indicates a slight NW-ward propagation of the tidal currents. However, the quantification of this propagation is difficult due to the large error bars and the small along-shelf distance between moorings.

Most tidal ellipses rotated CW and were mainly oriented NW–SE in the along-shelf direction.

Semi-minor axes were significant, indicating low eccentricity and suggesting that tidal currents play a key role in generating cross-shelf transport.

The tidal currents exhibited depth-dependent variations (Figs. 6 to 10), emphasising the baroclinic character of the tidal flow and suggesting the presence of an internal tide. In general, the amplitude of semidiurnal currents decreased with depth, while the diurnal currents remained relatively constant throughout the water column. This predominantly barotropic nature of the K1 currents is consistent with the observations of Kasajima and Svendsen (2002) on the Spitsbergen slope further north.

Near the surface, the drifter velocity statistics were similar to those of the moored ADCPs, although the variability was generally larger for the drifters (compare Tables 3 and 5). The standard deviation of drifter velocities at the southernmost mooring (CMRE4) reached 18 cm/s, with 42% of this variability attributed to K1 and M2 tidal currents (Table 6). The tidal ellipses derived from the drifter data were typically less eccentric and larger, especially for M2 on the shelf (see Fig. 12). These differences may be due to the influence of near-inertial motions, driven by local winds, which dominate the near-surface mixed layer. Since the experimental site lies just a few degrees north of the critical latitude for M2 waves, the close proximity of the semidiurnal and local inertial frequencies makes it challenging to distinguish between M2 tidal and inertial motions. In addition, the drifter results have large error bars due to the limited number of observations.

The WW collected temperature and salinity profiles for about two days (27–29 September 2019) near the PF on the shelf break (Fig. 13). The conservative temperature ranged from 3.5 °C at the surface to 7.4 °C between 10–40 m, then dropped to 4–5 °C at 200 m. The absolute salinity varied from 33.90 g/kg at the surface to 35.19–35.22 g/kg between 80–200 m. A mixed layer with homogeneous properties formed intermittently between 10–20 m, and deepened to 40–50 m on 29 September. The spiciness followed the temperature trends, with a surface minimum and a maximum at 40 m depth. A periodic signal with a ~12-hour period was observed, related to internal tides. The vertical isopycnal displacements reached up to 80 m (Fig. 15). The harmonic analysis revealed that the M2 tide dominated with an amplitude of 22 m at 140 m, and together with the K1 amplitude of 5 m, accounted for as much as 72% of the variability (Fig. 16).

The thermohaline properties were analysed in a T-S diagram (Fig. 14), showing variations in the upper 10–20 m, where fresher, colder ArW mixes with warmer, saltier AW. Below 80 m, salinity remained constant while temperature and density increased with depth.

From 22 September to 4 October 2019, three gliders were piloted along cross-shelf transects in the study area, targeting the surface PF observed in satellite imagery (Fig. 2). The glider transects, lasting 12 or 24 hours, revealed a surface layer of cold, relatively fresh ArW over warm AW, extending to ~100 m depth (Figs. 17 and 18). The water exhibited interleaving of ArW and AW, with meandering isopycnals influenced by temporal variations, including the tidal effects also observed in WW data. This interleaving made it difficult to discern a clear signature of the PF with depth. On the shelf, the coldest water was deeper, with maximum density indicating that it was both cold and salty.

The data of glider Anna and of WW were compared (Fig. 19), showing qualitative agreement, especially in detecting temperature changes on 29 September. The comparison showed that tidal effects influenced the temperature records, suggesting that temporal variations can introduce artificial spatial variability, particularly in temperature and density.

Thermohaline variability was analysed using glider data over 12 days across different locations separated by ~15 km in the along-shelf direction (Figs. 20 to 22). Glider Anna showed a near-surface temperature maximum offshore, with high variability at the surface and at intermediate depths (~60–120 m). Salinity increased with depth, with the highest variability occurring at the surface and near 50 m depth. Glider Maria showed similar patterns, with less pronounced cool surface water and clearer mid-depth temperature and offshore salinity maximum. Glider Dora Jr. showed more distinct thermohaline features, with temperature stable at around 50 m, and salinity increasing uniformly with depth. Surface variability was highest, decreasing offshore and with depth.

Despite the multi-platform approach adopted in NARVAL19, which included advanced instruments such as the WW and gliders, resolving the three-dimensional structure and temporal variability of thermohaline properties and currents SW of Spitsbergen remained a challenge. The proximity of inertial and M2 tidal frequencies hampered the separation of near-inertial and tidal currents, while the fine-scale (~1 km) water mass structure near the PF and tidal modulation resulted in undersampled and aliased spatial surveys. Nonetheless, this study provides a new descriptive perspective on the physical dynamics near the PF, and in particular highlights the role of cross-shelf tidal currents in mixing AW and ArW during their northward transport with the WSC, an important process for Arctic climate variability.

Acknowledgments. The data used in this study originate from the NARVAL19 sea trial, led by the French Naval Hydrographic and Oceanographic Service (SHOM), whose efforts are gratefully acknowledged. We extend our appreciation to the captain and crew of the research vessel *Pourquoi Pas?*, and to Pierre-Yves Le Moigne, Chief Scientist of NARVAL19, for their invaluable support. Special thanks go to Richard Stoner and Marina Ampolo Rella for their assistance with data collection, and to Elisa Cozzani for providing MATLAB scripts that facilitated onboard data processing. We are also grateful to Bartolomeo Garau, Craig Lewis, Daniele Cecchi, Giuliana Pennucci, and Silvia Falchetti for piloting the gliders. Lastly, we thank the Global Drifter Program, coordinated by Luca Centurioni, for kindly providing the surface velocity program barometer (SVPB) drifters. The major funding for this research was provided by the North Atlantic Treaty Organisation (NATO) Allied Command Transformation Future Solutions Branch.

REFERENCES

Bensi M., Kovačević V., Langone L., Aliani S., Ursella L., Goszczko I., Soltwedel T., Skogseth R., Nilsen F., Deponte D., Mansutti P., Laterza R., Rebesco M., Rui L., Lucchi R-G., Wåhlin A., Viola A., Beszczynska-Möller A. and Rubino A.; 2019: *Deep flow variability offshore south-west Svalbard (Fram Strait).* Water, 11, 683, doi: 10.3390/w11040683.

Boyd T.J. and D'Asaro E.A.; 1994: *Cooling of the west Spitsbergen current: wintertime observations west of Svalbard.* J. Geophys. Res., 99, 22597-22618, doi: 10.1029/94JC01824.

Feistel R.; 2012*: TEOS-10: a new international oceanographic standard for seawater, ice, fluid water and humid air.* Int. J. Thermophys., 33, 1335-1351, doi: 10.1007/s10765-010-0901-y.

Gascard J.-C., Richez C. and Rouault C.; 1995: *New insights on large-scale oceanography in Fram Strait: the west Spitsbergen current.* Smith W.O. and Grebmeir J.M. (eds.), Arctic Oceanography: marginal ice zones and continental shelves, doi: 10.1029/CE049p0131.

Gjevik B., Nøst E. and Straume T.; 1994: *Model simulations of the tides in the Barents Sea.* J. Geophys. Res., 99, 3337-3350, doi: 10.1029/93JC02743.

Kasajima Y. and Svendsen H.; 2002: *Tidal features in the Fram Straits.* Cont. Shelf Res., 22, 2461-2477, doi: 10.1016/S0278-4343(02)00132-2.

Koszalka I., LaCasce J.H., Andersson M., Orvik K.A. and Mauritzen C.; 2011: *Surface circulation in the Nordic Seas from clustered drifters.* Deep-Sea Res., Part I, Oceanogr. Res. Pap., 58, 468-485, doi: 10.1016/j.dsr.2011.01.007.

Kowalik Z. and Proshutinsky A.Y.; 1993: *Diurnal tides in the Arctic Ocean.* J. Geophys. Res., 98, 16449-16468, doi: 10.1029/93JC01363.

Kowalik Z. and Marchenko A.; 2023: *Tidal motion enhancement on Spitsbergen Bank, Barents Sea.* J. Geophys. Res., 128, e2022JC018539, doi: 10.1029/2022JC018539.

Loeng H.; 1991: *Features of the physical oceanographic conditions of the Barents Sea.* Polar Res., 10, 5-18, doi: 10.3402/polar.v10i1.6723.

Lumpkin R. and Pazos M.; 2007: *Measuring surface currents with surface velocity program drifters: the instrument, its data and some results.* Mariano A., Rossby T. and Kirwan D. (eds), In Chapter 2: Lagrangian analysis and prediction of coastal and ocean dynamics, Cambridge Univ. Press, Cambridge, UK, pp. 39-67.

McDougall T.J. and Krzysik O.A.; 2015: *Spiciness.* J. Mar. Res., 73, 141-152.

Niiler P.P.; 2001: *The world ocean surface circulation.* In: Siedler G., Church J. and Gould J. (eds), Ocean circulation and climate: observing and modelling the global ocean, Int. Geophys., 77, 193-204, doi: 10.1016/S0074-6142(01)80119-4.

Nilsen, F., Skogseth, R., Vaardal-Lunde J. and Inall M.; 2016: *A simple shelf circulation model: intrusion of Atlantic water on the west Spitsbergen shelf.* J. Phys. Oceanogr., 46, 1209-1230, doi: 10.1175/JPO-D-15-0058.1.

Orvik K.A. and Niiler P.; 2002*: Major pathways of Atlantic water in the northern North Atlantic and Nordic Seas toward Arctic.* Geophys. Res. Lett., 29, 1896, doi: 10.1029/2002GL015002.

Padman L. and Erofeeva S.; 2004: *A barotropic inverse tidal model for the Arctic Ocean.* Geophys. Res. Lett., 31, L02303, doi: 10.1029/2003GL019003.

Pawlowicz R., Beardsley B. and Lentz S.; 2002: *Classical tidal harmonic analysis including error estimates in MATLAB® using T_TIDE.* Comput. Geosci., 28, 929-937.

Pinkel R., Goldin M.A., Smith J.A., Sun O.M., Aja A.A., Bui M.N. and Hughen T.; 2011: *The wirewalker: a vertically profiling instrument carrier powered by ocean waves.* J. Atmos. Ocean. Tech., 28, 426-435, doi: 10.1175/2010JTECHO805.1.

Poulain P.-M.; 2024: *Unveiling near-inertial wave dynamics and storm-driven currents: insights from moorings in the coastal Mediterranean Sea.* Cont. Shelf Res., 282, 105321, doi: 10.1016/j.csr.2024.105321.

Poulain P.-M.; 2025: *Statistical analysis of tidal currents based on surface drifter observations: application to the Barents Sea and the waters around the Svalbard Archipelago.* J. Atmos. Oceanic Technol., 42, 567-586, doi: 10.1175/JTECH-D-24-0126.1.

Poulain P.-M., Warn-Varnas A. and Niiler P.P.; 1996: *Near-surface circulation of the Nordic seas as measured by Lagrangian drifters*. J. Geophys. Res.: Oceans, 101, 18237-18258, doi: 10.1029/96JC00506.

Poulain P.-M., Stoner R., Lewis C., Ampolo-Rella M. and Cozzani E.; 2019: *Testing the Wirewalker profiling system for high-frequency underwater dynamics characterization*. CMRE Memorandum Rep., CMRE-MR-2019-022, La Spezia, Italy, 32 pp.

Poulain P.-M., Pennucci G. and Lewis C.; 2020: *High-frequency dynamics south-west of Svalbard.* CMRE Memorandum Rep., CMRE-MR-2020-002, La Spezia, Italy, 59 pp.

Poulain P.-M., Oddo P., Pennucci G., Lewis C., Sliwka J., Duda T.F. and Drago A.; 2023: *Observations of internal tidal dynamics southwest of Malta in the central Mediterranean Sea*. Cont. Shelf Res., 254, 104922, doi: 10.1016/j.csr.2022.104922.

Quadfasel D., Gascard J.-C. and Koltermann K.-P.; 1987: *Large-scale oceanography in Fram Strait during the 1984 Marginal Ice Zone Experiment.* J. Geophys. Res., 92, 6719-6728, doi: 10.1029/JC092iC07p06719.

Rainville L. and Pinkel R.; 2001: *Wirewalker: an autonomous wave-powered vertical profiler.* J. Atmos. Ocean. Tech., 18, 1048-1051.

Saloranta T.M. and Svendsen H.; 2001: *Across the Arctic front west of Spitsbergen: high-resolution CTD sections from 1998-2000.* Polar Res., 20, 177-184, doi: 10.3402/polar.v20i2.6515.

Teigen S.H., Nilsen F. and Gjevik B.; 2010: *Barotropic instability in the west Spitsbergen current.* J. Geophys. Res., 115, C07016, doi: 10.1029/2009JC005996.

Teigen S.H., Nilsen F., Skogseth R., Gjevik B. and Beszczynska-Möller A.; 2011: *Baroclinic instability in the west Spitsbergen current*. J. Geophys. Res., 116, C07012, doi: 10.1029/2011JC006974.

Von Appen W.-J., Schaue U., Hattermann T. and Beszczynska-Möller A.; 2016: *Seasonal cycle of mesoscale instability of the west Spitsbergen current.* J. Phys. Oceanogr., 46, 1231-1254, doi: 10.1175/JPO-D-15-0184.1

Yuill R.S.; 1971: *The standard deviational ellipse: an updated tool for spatial description.* Geografiska Annaler, Series B, Hum. Geogr., 53, 28-39, doi: 10.2307/490885.

Corresponding author: Pierre-Marie Poulain
National Institute of Oceanography and Applied Geophysics
Borgo Grotta Gigante, 42/c 34010 Sgonico (Trieste), Italy
Phone: +39 0402140201; e-mail: ppoulain@ogs.it

Appendix

The harmonic analysis can only accurately distinguish the primary tidal constituents (O1, K1, M2, and S2) if the time series extends beyond 14.77 days. For shorter observation periods, spectral leakage between constituents may occur, leading to a potential over- or underestimation of amplitudes due to the influence of the spring-neap tidal cycle.

During the NARVAL19 sea trial, data from the moored instrument were collected over periods of 10 to 15 days. When applying harmonic analysis to a common observation period of ~10 days, the separation of K1 and M2 constituents is likely to be influenced by contamination from other constituents, such as O1 and S2. Since the observation period is nearly centred around the New Moon and spring tide (see Fig. 5), some overestimation of the amplitudes is to be expected.

To quantify this effect, we applied the t_tide harmonic analysis to velocity measurements of mooring SHOM3 at 40 m depth and compared the results of the full 15.18-day time series with those of the restricted 10.46-day common period. The results, presented in Table A1, illustrate the discrepancies when using 4, 2, and 1 constituents in the analysis.

As expected, a shorter observation period leads to a higher percentage of variance explained by the tidal model, reaching a maximum of 33% when four constituents are used. The semi-major axis amplitudes of both K1 and M2 are larger when the shorter common period is used compared to the full time series. For M2, the overestimation due to S2 leakage is up to 1 cm/s, while the increase for K1 is smaller, up to 0.28 cm/s.

In contrast, the semi-minor axes of K1 and M2 decrease when using the shorter common period. Inclination and phase variations remain within 10°. Moreover, the amplitude differences between the analyses using t_tide with 4, 2, or 1 constituents do not exceed 0.1 cm/s.

In conclusion, the results of the harmonic analysis for K1 and M2, which are based on an observation period of ~10 days, are overestimated by up to 1 cm/s due to the timing of the observations coinciding with the spring tide. The tidal ellipses also appear more eccentric, with inclination and phase differences remaining within 10°.

Table A1 - Results of the harmonic analysis applied to the currents at 40 m for the mooring SHOM3 using the common period (starting on 26 September 2019 17:01:45 UTC) and using all the available data starting on 22 September 2019 06:29:15 UTC.

SHOM3	**Common period starting on 26 September 2019 17:01:45 UTC (10.46 days)**					**Full period starting on 22 September 2019 06:29:15 (UTC) (15.18 days)**				
Tidal const.	Semi-major [cm/s]	Semi-minor [cm/s]	Inc. [°]	Phase [°]	Exp. var. [%]	Semi-major [cm/s]	Semi-minor [cm/s]	Inc. [°]	Phase [°]	Exp. var. [%]
O1	0.40	0.01	138	48		1.64	-0.83	170	154	
K1	5.86	-2.97	152	151	33	5.58	-3.12	156	169	29
M2	10.12	-2.29	28	202		9.34	-2.47	19	195	
S2	1.77	-0.46	46	331		3.67	-1.74	61	323	
K1	5.80	-3.03	152	152	33	5.72	-3.17	156	169	26
M2	10.41	-2.21	29	205		9.37	-2.53	19	195	
M2	10.43	-2.09	28	204	24	9.35	-2.49	19	195	18